Effect of Strained $k \cdot p$ Deformation Potentials on Hole Inversion-Layer Mobility

Ming-Jer Chen, *Senior Member, IEEE*, Chien-Chih Lee, and Wan-Li Chen

***Abstract*—In the literature dedicated to strained p-type metal–oxide–semiconductor field-effect transistor inversion-layer mobility calculation via a $k \cdot p$ valence-band structure, three key strain-related material parameters, namely, the Bir–Pikus deformation potentials a_v, b, and d, were widespread in magnitude. To improve such large discrepancies, in this paper, we conduct sophisticated calculations on $\langle 110\rangle/(001)$ and $\langle 110\rangle/(110)$ hole inversion-layer mobility for gigapascal-level uniaxial stresses along each of three crystallographic directions. The screening effect on surface roughness scattering is taken into account. We find that, to affect the calculated hole mobility enhancement, a_v is weak, b is moderate, and d is strong, particularly for the uniaxial compressive stress along the $\langle 110\rangle$ direction. This provides experimental guidelines for an optimal determination of the primary factor, i.e., d, and the secondary factor, i.e., b, with the commonly used values for a_v. The result remains valid for varying surface roughness parameters and models and is supported by recent first-principles and tight-binding calculations. Thus, the strained $k \cdot p$ valence-band structure with the optimized deformation potentials can ensure the accuracy of the calculated transport properties of 2-D hole gas under stress.**

***Index Terms*—Bir–Pikus, deformation potential, hole, $k \cdot p$, metal–oxide–semiconductor field-effect transistors (MOSFETs), mobility, simulation, strain, stress, tight-binding.**

I. Introduction

THE valence-band structure in the inversion layers of silicon p-type metal–oxide–semiconductor field-effect transistors (pMOSFETs) can be obtained by self-consistently solving Poisson's and Schrödinger's equations as originally demonstrated by Bangert *et al.* [1] and by Ohkawa and Uemura [2]. Then, it is a straightforward task to furnish 2-D hole transport properties. This also is the case for state-of-the-art pMOSFETs undergoing strain engineering in the manufacturing process. Specifically, to compensate for the mobility degradation in a scaling direction [3], gigapascal-level stresses [4], [5] are needed. To match this trend, it is crucial to accurately calculate the hole inversion-layer mobility in the highly strained valence-band structure, particularly the $k \cdot p$ one originating from the works of Luttinger and Kohn [6] and of Bir and Pikus [7]. So far, however, published calculation results in the context of the strained $k \cdot p$ valence-band structure differed much from each other [8]–[11], as shown in Fig. 1.

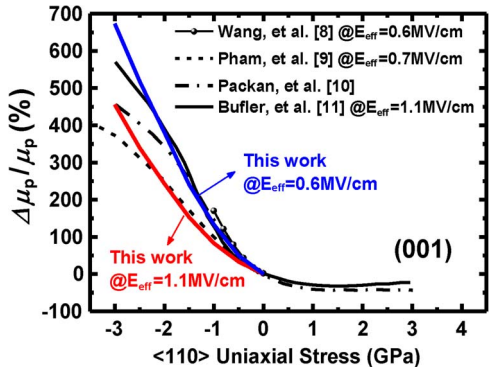

Fig. 1. Calculated $\langle 110\rangle$ hole inversion-layer mobility change, from [8]–[11] and this paper, plotted versus $\langle 110\rangle$ uniaxial stress on the (001) substrate.

TABLE I
List of Scattering Parameters and Bir–Pikus Parameters Used in Fig. 1

	D_{ac} (eV)	D_{op} (10^8eV/cm)	$\hbar\omega_{op}$ (meV)	λ (nm)	Δ (nm)	a_v (eV)	b (eV)	d (eV)	E_{eff} (MV/cm)
This Work N_{sub}=1x10^{17}cm^{-3} T=300K	5.62	8.5	61.2	2.6	0.42	2.46	-2.1	-3.1	0.6 / 1.1
Wang, *et al.* [8]	9.64	12.72	65	2.0	0.758	2.1	-1.6	-2.7	0.6
Bufler, *et al.* [11]	NA	NA	NA	NA	NA	2.46	-2.35	-5.32	1.1

D_{ac} is the average acoustic deformation potential; D_{op} the average optical deformation potential; $\hbar\omega_{op}$ the optical phonon energy; λ the surface roughness correlation length; and Δ the surface roughness rms height.

Such inconsistencies are likely due to largely spanned values [8], [11] (see Table I) in the Bir–Pikus deformation potentials, namely, the hydrostatic valence-band deformation potential a_v, the uniaxial $\langle 100\rangle$ deformation potential b, and the uniaxial $\langle 111\rangle$ deformation potential d. Indeed, according to literature sources (see [12]–[15] and the references therein), a_v, b, and d were widespread in terms of the error range: 2.06 eV $\leq a_v \leq$ 2.46 eV, -2.58 eV $\leq b \leq -1.5$ eV, and -5.3 eV $\leq d \leq -3.1$ eV. There were two origins proposed [13] for such large errors. First, a complicated dependence on the strain conditions exists in nature, making the extraction of deformation potentials a hard problem. Second, the strain range used in the extraction procedure was limited; for example, $b = -2.33$ eV and $d = -4.75$ eV [13] were representative of small-strain situations, and deviations should be expected at large strain, according to Fischetti and Laux [13].

Manuscript received October 15, 2012; revised January 11, 2013; accepted January 28, 2012. Date of current version March 20, 2013. This work was supported by the National Science Council of Taiwan under Contract NSC 100-2221-E-009-017-MY3. The review of this paper was arranged by Editor R. Huang.

M.-J. Chen is with the Department of Electronics Engineering and the Institute of Electronics, National Chiao Tung University, Hsinchu 300, Taiwan (e-mail: chenmj@faculty.nctu.edu.tw).

C.-C. Lee and W.-L. Chen were with the Department of Electronics Engineering, NCTU, and are currently with the Taiwan Semiconductor Manufacturing Company (TSMC), Hsinchu 300, Taiwan.

Color versions of one or more of the figures in this paper are available online at http://ieeexplore.ieee.org.

Digital Object Identifier 10.1109/TED.2013.2244896

On the other hand, good agreement with the mobility enhancement data can be obtained with the different values of a_v, b, and d (see Table I for the work of Wang *et al.* [8]); however, the corresponding applied uniaxial stress range was quite limited (less than 400 MPa in magnitude; see [8, Fig. 18]). Even the primary factors and guidelines needed to experimentally determine the unique values of a_v, b, and d were not published, in particular, in the gigapascal-level stress range. Importantly, two additional factors, whose significance was overlooked or not explicitly reported in the literature [8]–[11], are needed to be taken into account. One is the acoustic deformation potential $D_{\rm ac}$. $D_{\rm ac}$ is not an independent parameter but a function of a_v, b, and d, according to Bir and Pikus [7], Tiersten [16], and Lawaetz [17]. The second additional factor is the deformation potential of optical phonons d_0 or the average optical deformation potential $D_{\rm op}$, which will affect the choice of surface roughness parameters or models (exponential and Gaussian) in the mobility data fitting.

In this paper, we employ a strained $k \cdot p$ mobility calculation method under gigapascal-level stress conditions, with an aim to determine the primary factors responsible and, hence, the guidelines. The significance of $D_{\rm ac}$ and $D_{\rm op}$ is demonstrated in the mobility data fitting. The validity and applicability of the strained $k \cdot p$ valence-band structure with the experimentally determined deformation potentials in this paper are addressed as well.

II. Calculation Method and Scattering Models

A. Calculation Method

We started the task by incorporating the strain Hamiltonian [7] to a previously established six-band $k \cdot p$ computational booster [18] and by adding a subsequent self-consistent solving of Poisson's and Schrödinger's coupled equations with the strain Hamiltonian included. This sophisticated integration constitutes a computationally efficient self-consistent strained $k \cdot p$ solver. The outcomes of the solver contain the hole subband energy level, the Fermi level, the wave function, the density-of-states (DOS) function, and the strained $E-k$ structure. Then, the hole inversion-layer mobility can be calculated using the Kubo–Greenwood formula [19]–[21], i.e.,

$$\mu_{xx} = \frac{e}{4\pi^2 k_B T P_{\rm inv}} \sum_{\mu} \int d^2\boldsymbol{k} v_x^{\mu}(\boldsymbol{k}) \times v_x^{\mu}(\boldsymbol{k}) \times \tau_{\rm total}^{\mu}(\boldsymbol{k}) \times f_0(\boldsymbol{k}) \left(1 - f_0(\boldsymbol{k})\right) \quad (1)$$

where e is the free electron charge, $P_{\rm inv}$ is the total hole density per unit area, v_x^{μ} is the group velocity of subband μ along x-direction, and f_0 is the Fermi–Dirac distribution function in equilibrium. Under the momentum relaxation time approximation, the total scattering time $\tau_{\rm total}^{\mu}$ of subband μ in (1) can relate to acoustic phonon scattering, optical phonon scattering, and surface roughness scattering, all through the expression

$$\frac{1}{\tau_{\rm total}^{\mu}(\boldsymbol{k})} = \frac{1}{\tau_{\rm ac}^{\mu}(\boldsymbol{k})} + \frac{1}{\tau_{\rm op}^{\mu}(\boldsymbol{k})} + \frac{1}{\tau_{\rm sr}^{\mu}(\boldsymbol{k})}.$$

In this paper, eighteen lowest subbands were used in the mobility calculation. This is reasonable because we found that these subbands occupy most of the population, particularly the stress case. In addition, the eighteenth subband energy for the unstressed case at 1 MV/cm is 0.407 eV above the surface valence-band edge. The critical parameters used, such as the Luttinger parameters, the split-off hole energy, the elastic constants, and the Bir–Pikus deformation potentials, are all listed in Table II. Without loss of generality, the substrate doping concentration $N_{\rm sub}$ was set to 1×10^{17} cm^{-3} with the temperature at 300 K.

TABLE II
Material Parameters Used in This Paper

γ_1	γ_2	γ_3	a_v (eV)	b (eV)	d (eV)	d_0 (eV)	$\Delta_{split\text{-}off}$ (eV)
4.285	0.339	1.446	2.46	-2.1	-3.1	26.6	0.044
c_{11}	c_{12} (10^{10} N/m^2)	c_{44}	ρ (g/cm^3)	a_0 (Å)	v_l (10^5 cm/sec)	v_t	
16.6	6.41	7.94	2.329	5.43	9.04	5.41	

γ_1, γ_2, and γ_3 are Luttinger parameters; a_v, b, and d are the Bir-Pikus potentials; d_0 is the optical deformation potential; $\Delta_{split\text{-}off}$ is the split-off hole energy; c_{11}, c_{12}, and c_{44} are the elastic coefficients; ρ and a_0 are the crystal density and lattice constant of silicon; v_l and v_t are the longitudinal and transverse sound velocity.

B. Acoustic Phonon Scattering

We followed the isotropic treatment by Fischetti *et al.* [22] concerning acoustic phonon scattering but did not take into account the inelastic and dielectric screening effects of acoustic phonons in this paper. The critical parameter, namely, the acoustic deformation potential $D_{\rm ac}$, is strongly connected to Bir–Pikus deformation potentials [7], [16], [17]. According to Lawaetz [17], $D_{\rm ac}$ can be formulated as

$$\begin{aligned} D_{\rm ac}^2 &= a_v^2 + c_l/c_t \left(b^2 + \frac{1}{2}d^2\right) \\ c_l &= \frac{(3c_{11} + 2c_{12} + 4c_{44})}{5} \\ c_t &= \frac{(c_{11} - c_{12} + 3c_{44})}{5} \end{aligned} \quad (2)$$

where c_l and c_t are the average longitudinal and transverse elastic coefficients, respectively. c_{11}, c_{12}, and c_{44} are the elastic coefficient elements, whose values are listed in Table II. The elastic acoustic phonon scattering rate model used in this paper is

$$\frac{1}{\tau_{\rm ac}^{\mu}(\boldsymbol{k})} = \frac{2\pi k_B T D_{\rm ac}^2}{\hbar \rho v_l^2} \sum_{v} F_{v\mu} {\rm DOS}_v\left(E_{\mu}(\boldsymbol{k})\right) \quad (3)$$

where $F_{v\mu}$ is equal to $\int |\xi_0^{\mu}(z) \cdot \xi_0^{\nu *}(z)|^2 dz$, i.e., the wavefunction $\xi_0(z)$ overlap integral between the initial subband μ and the final subband ν. ρ and v_l denote the crystal density and the longitudinal sound velocity, respectively. Both intra- and intersubband acoustic phonon scattering were considered in this paper.

C. Optical Phonon Scattering

Optical phonon scattering involves the absorption and emission of optical phonons with the exchange of energy (61.2 meV in this paper). According to Wiley [23] and Costato and

Reggiani [24], the optical deformation potential $D_{\rm op}$ can have the following formalism:

$$D_{\rm op}^2 = \frac{c_l + 2c_t}{\rho \bar{v}_s^2} \left(\frac{d_0}{a_0}\right)^2 \tag{4}$$

where a_0 is the lattice constant, d_0 is the deformation potential of optical phonons, and $\bar{v}_s$ is the average sound velocity consisting of the longitudinal and transverse sound velocities, i.e., v_l and v_t, respectively, with the formulation of $\bar{v}_s^2 = (v_l^2 + 2v_t^2)/3$. Then, the isotropic absorbing and emitting optical phonon scattering rate can be written as

$$\frac{1}{\tau_{\rm op}^{\mu}(\boldsymbol{k})} = \frac{\pi D_{\rm op}^2}{\rho \omega_{\rm op}} \sum_{\upsilon} F_{\upsilon\mu} {\rm DOS}_{\upsilon} \left(E_{\upsilon}(\boldsymbol{k}) \mp \hbar\omega_{\rm op}\right) \times \frac{1 - f_0\left(E_{\mu}({\rm k}) \mp \hbar\omega_{\rm op}\right)}{1 - f_0\left(E_{\mu}(\boldsymbol{k})\right)} \times \left(n_{\rm op} + \frac{1}{2} \pm \frac{1}{2}\right) \tag{5}$$

where

$\omega_{\rm op}$ optical phonon frequency;
$n_{\rm op}$ Bose occupation factor of optical phonons.

Equation (5) features both intra- and intersubband optical phonon scattering but with no screening effect in this paper.

D. Surface Roughness Scattering

To deal with surface roughness scattering, we first followed Pham *et al.* [25] and De Michielis *et al.* [26], to take only the intrasubband scattering. Then, the screening effect in the dielectric function, as formulated by Yamakawa *et al.* [27] and Gámiz *et al.* [28], was incorporated into the surface roughness scattering rate expression in the context of the exponential autocovariance function

$$\frac{1}{\tau_{\rm sr}^{\mu}(\boldsymbol{k})} = \frac{2\pi^2 \Delta^2 \lambda^2}{\hbar} \sum_{\upsilon} \frac{\left(\boldsymbol{\Gamma}_{\rm eff}^{\mu,\upsilon}\right)^2}{(2\pi)^2} \int \delta\left(E_{\upsilon}(\boldsymbol{k}') - E_{\mu}(\boldsymbol{k})\right) \times \frac{(1 - \cos\theta)}{\epsilon(q) \times \left(1 + \frac{q^2\lambda^2}{2}\right)^{1+n}} d^2k' \tag{6}$$

where

Δ RMS height of the amplitude of the surface roughness;
λ correlation length of the surface roughness;
q $q = |\boldsymbol{k}' - \boldsymbol{k}|$;
θ angle between $\boldsymbol{k}'$ and $\boldsymbol{k}$;
n adjustable factor ($= 1/2$ in this paper);
$\boldsymbol{\Gamma}_{\rm eff}^{\mu,\upsilon}$ $\boldsymbol{\Gamma}_{\rm eff}^{\mu,\upsilon} = \int (\xi_0^{\nu *}(z) \cdot \xi_0^{\mu}(z) \cdot deV(z)/dz + E_{\nu}^{(0)} \cdot \xi_0^{\nu *}(z) \cdot d\xi_0^{\mu}(z)/dz - E_{\mu}^{(0)} \cdot d\xi_0^{\nu *}(z)/dz \cdot \xi_0^{\mu}(z))dz$;
$E_{\nu}^{(0)}$ energy minimum of subband ν;
$\epsilon(q)$ static wave-vector-dependent dielectric function;
$\epsilon(q)$ $= 1 + (e^2/2\epsilon_{\rm Si}\epsilon_0)(F(q)/q) \int (\delta(E_{\nu}(k') - E_{\mu}(k))d^2k')/(2\pi)^2$;
$F(q)$ $= \sum_{\upsilon} \int dz \int dz' |\xi_0^{\nu}(z)|^2 |\xi_0^{\nu}(z)|^2 e^{-q|z-z'|}$.

Importantly, (6) has the ability to adequately handle the angular dependence of surface roughness scattering, as shown in Fig. 2, in terms of the calculated unscreened and screened scattering rates versus hole energy for the (001) substrate. It can be seen from the figure that the scattering angular is more pronounced for gigapascal-level stress. Fig. 2 also reveals the significance of the screened surface roughness scattering (see [28] and references therein); that is, the screening effect gives rise to a decrease in surface roughness scattering and, hence, an increase in surface roughness limited mobility, regardless of stress. Unless stated otherwise, in the subsequent sections, the screening effect on surface roughness scattering is taken into account.

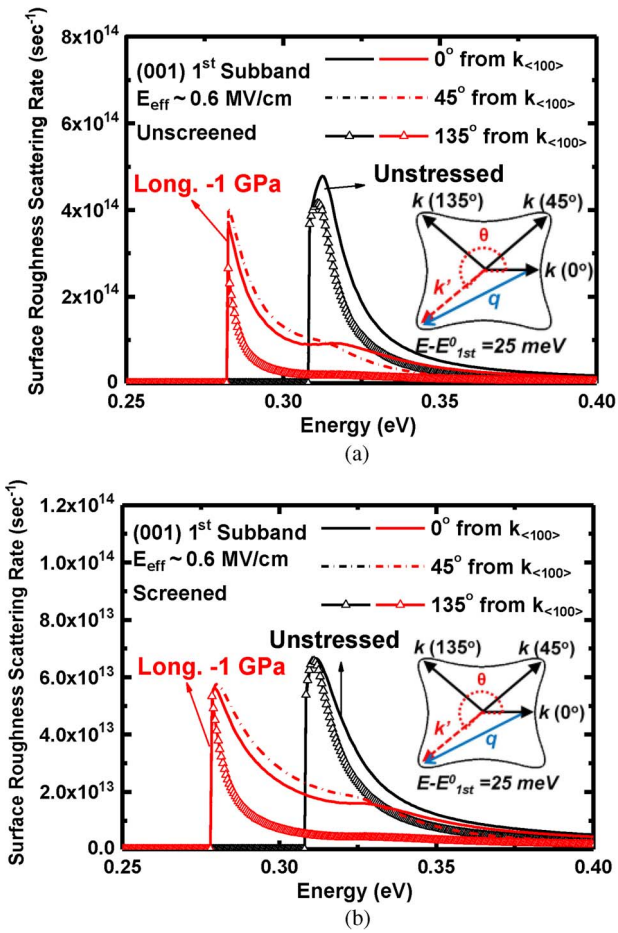

Fig. 2. Calculated (a) unscreened and (b) screened intrasubband surface roughness scattering rates along different k-directions of the first subband of the (001) substrate with and without the longitudinal -1-GPa stress. The obvious angular dependence can be found in both cases.

III. Effect of Bir–Pikus Deformation Potentials

Calculations with the different values of Bir–Pikus parameters were executed for each of the following three distinct uniaxial stress directions: 1) in-plane longitudinal stress along the transport $\langle 110 \rangle$ direction; 2) in-plane transverse stress perpendicular to the transport $\langle 110 \rangle$ direction; and 3) out-of-plane stress in the quantum confinement direction. The results on both (001) and (110) substrates are shown in Fig. 3 for two cases: one of $a_v = 2.46$ eV, $b = -2.1$ eV, and $d = -4.8$ eV (close to that of [11]); and one of $a_v = 2.1$ eV, $b = -1.6$ eV, and $d = -2.7$ eV (as in [8]). The calculated 3-D uniaxial stress dependency of mobility change all resemble those published elsewhere [10], [11]. This confirms the validity of the calculation method in this paper. In Fig. 3, one can see that different Bir–Pikus parameters lead to different strain altered hole mobilities, particularly for the longitudinal compressive stress.

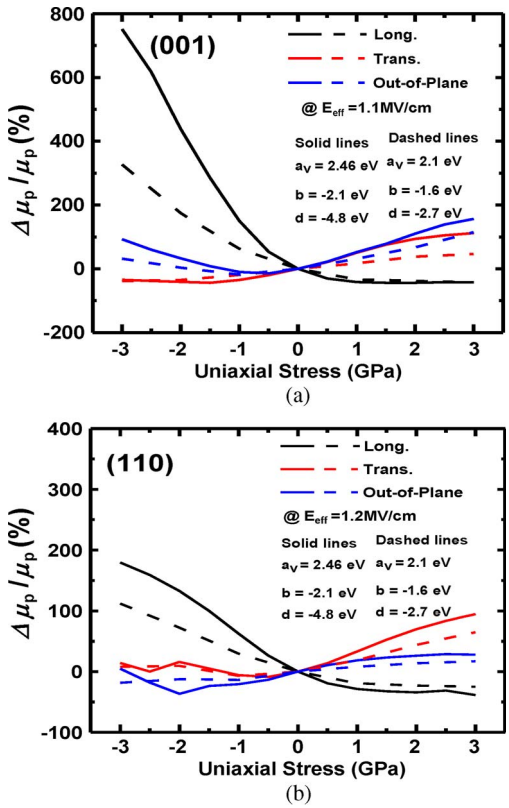

Fig. 3. Calculated 3-D uniaxial stress dependence of hole inversion-layer mobility change for the (a) (001) and (b) (110) substrates.

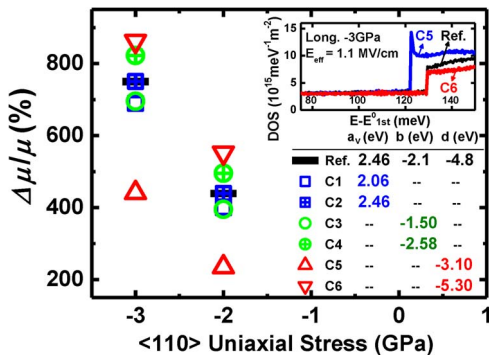

Fig. 4. Calculated hole inversion-layer mobility enhancement values at two uniaxial compressive stresses for the reference deformation potentials and six different conditions (C1–C6). (Inset) Calculated DOS of two lowest subbands for three conditions, namely, reference, C5, and C6.

To determine the primary factors, we made a set of $a_\upsilon = 2.46$ eV, $b = -2.1$ eV, and $d = -4.8$ eV as reference. In the subsequent calculation, one of these parameters is given three distinct values (one reference and two values equal or close to the upper and lower limits of the aforementioned error range), along with the two remainders fixed at their reference values. The results are plotted in Fig. 4 for two $\langle 110 \rangle$ uniaxial stresses of -2 and -3 GPa on the (001) substrate. Note that different sets of a_υ, b, and d produce different calculated $D_{\rm ac}$ values according to (1), which will *together* alter the amount of the mobility change percentage. It is further shown in Fig. 4 that a change in a_υ only has a weak effect on mobility enhancement; the effect of varying b is moderate, but for d, its effect is strongly large. The origin is due to the decreased subband separation and the increased DOS, as shown in the inset in the figure. The primary factor d and the secondary factor b also hold for the (110) case (not shown here). The corresponding first-subband effective masses near the Gamma point along the $\langle 100 \rangle$ and $\langle 110 \rangle$ directions and the subband levels are listed in Table III for different a_υ, b, and d groups (reference and C1–C6 in Fig. 4) under the longitudinal compressive stress of 3 GPa in magnitude. It can be seen that a_υ (C1 and C2) only affects the valence-band shift, whereas for b and d (C3–C6), both the valence-band shift and shape are changed, similar to the well-known impacts of γ_1, γ_2, and γ_3 on the valence-band structure.

TABLE III
C1–C6 ALTERED EFFECTIVE MASS AND SUBBAND LEVEL CHANGE

1st Subband @ Long. -3GPa	$m^*_{<100>}$	$m^*_{<110>}$	$\Delta E_{1st}{}^0$ (meV)
Ref.	0.32 m_0	0.18 m_0	$E_{1st}{}^0$=393
C1	+0%	+0%	-4.7
C2	+0%	+0%	+4.5
C3	-0.3%	+4.4%	+5.9
C4	+0.4%	-3.5%	-5.9
C5	-0.3%	+6.3%	+28.9
C6	-0.1%	-3.0%	-16.0

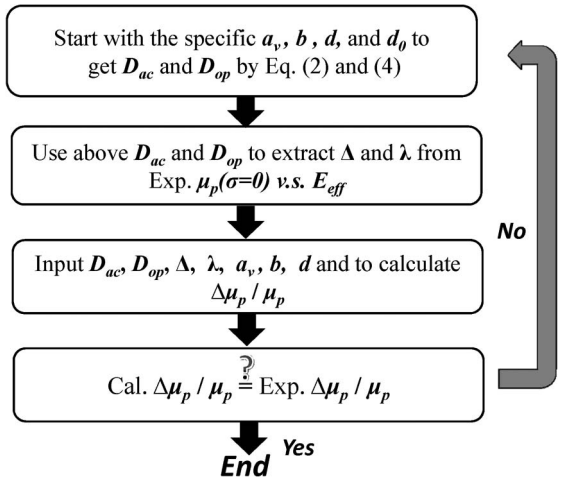

Fig. 5. Flowchart showing the establishment of the guidelines with the mutual coupling between the Bir–Pikus deformation potentials and $D_{\rm ac}$ taken into account.

IV. GUIDELINES AND EXPERIMENTAL DETERMINATION

Guidelines are established in terms of a flowchart shown in Fig. 5. There are six input parameters, namely, a_υ, b, d, d_0, Δ, and λ. The corresponding $D_{\rm ac}$ and $D_{\rm op}$ can be determined according to (2) and (4), respectively. To facilitate the procedure, we first took a literature value of 26.6 eV for d_0 [29] and, hence, the corresponding $D_{\rm op}$ of 8.5×10^{-8} eV/cm. Then, a fit to the experimental unstrained hole effective mobility data in Fig. 6, as cited elsewhere [30], was carried out, producing $\Delta = 0.42$ nm and $\lambda = 2.6$ nm. It can be seen from the figure that a good fitting appears in the high $E_{\rm eff}$ region, or the universal mobility region, which is valid for different substrate orientations and different transport directions. This validates the presented calculation method. Here, $E_{\rm eff}$ is the vertical effective electric field in the inversion layer, which was calculated using

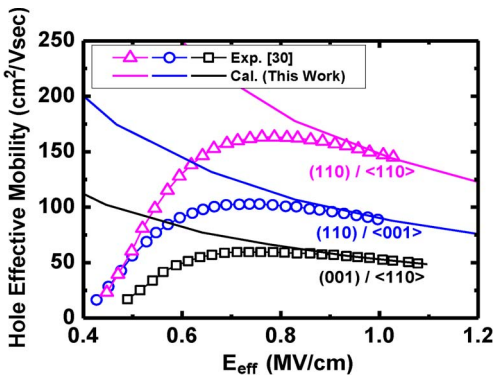

Fig. 6. Comparison of (symbols) experimental hole inversion-layer effective mobility [30] and (lines) calculated hole universal mobility versus vertical effective electric field. The scattering parameters used are listed in Table I and apply to both (001) and (110) substrates.

the empirical formula $E_{\rm eff} = e(\eta P_{\rm inv} + P_{\rm dep})$ with η taken as 1/3 according to Takagi *et al.* [31], where $P_{\rm inv}$ is the inversion-layer density, and $P_{\rm dep}$ is the substrate depletion charge density. Deviations in the low $E_{\rm eff}$ region are expected because impurity Coulomb scattering was not taken into account in this paper.

At this point, the number of input parameters reduces to three. Since a_v and b are weak or moderate in effect, we can quote the literature values $a_v = 2.46$ eV [13] and $b = -2.1$ eV [14]. Then, with a guess of d, the strain induced hole mobility change was calculated; an updated d was obtained in comparison with the experimental data. This process was iterated until a good fitting is achieved. This way, we obtained $d = -3.1$ eV and $D_{\rm ac} = 5.8$ eV from a fit to hole inversion-layer mobility enhancement data under uniaxial compressive stress [4], [5], as depicted in Fig. 7(a). Note that the corresponding $E_{\rm eff}$ of around 1 MV/cm was estimated under a gate overdrive of -0.75 V [4], [5]. Biaxial-stress mobility data [32], [33] also were quoted. Extra calculation for this case was performed. The result is shown in the inset in the figure. Fairly good agreement remains, without changing any parameters. The extracted results are listed in Table I. The corresponding calculated hole mobility change at two different $E_{\rm eff}$ is shown in Fig. 1 for comparison.

Even making a change of b to -1.6 eV, we found that the reproduction quality is acceptable, as shown in the inset in Fig. 7. Strikingly, such change in b does not significantly affect the calculated hole mobility enhancement in case of uniaxial stress, as shown in Fig. 7. This invariability supports the published error range of -2.58 eV $\le b \le -1.5$ eV [12]–[15]. The preceding arguments hold for other a_v values, as has been proved in Fig. 4. This can reasonably explain the commonly used values of 2.06 eV $\le a_v \le$ 2.46 eV [12], [15]. These optimized parameters hold in the (110) case, as shown in Fig. 7(b).

The preceding results stemmed from a specific d_0 of 26.6 eV. As illustrated by the guidelines in Fig. 5, a change in d_0 may change the extracted surface roughness parameters. In fact, the quoted mobility data sources [4], [5], [30], [32], [33] came from different manufacturing processes featuring different surface roughness details. Thus, it is clear that the uncertainty exists in d_0 or, equivalently, the surface roughness parameters. To reflect this, we show in Fig. 8(a) the effect of varying surface roughness height Δ with its correlation length λ fixed at 2.6 nm.

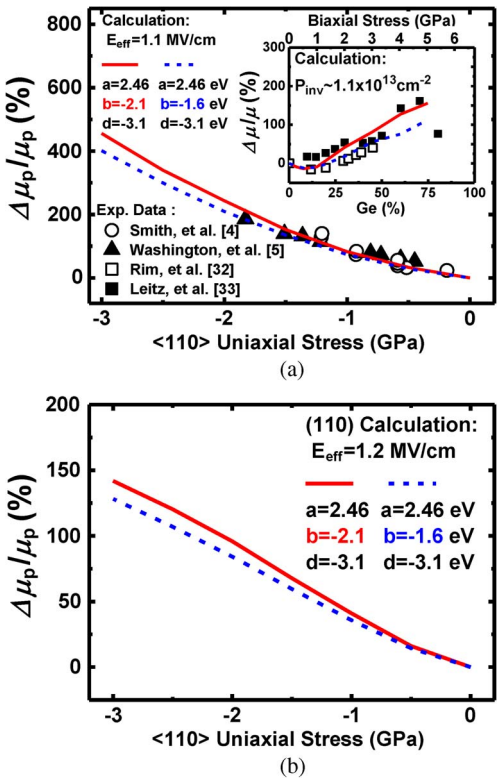

Fig. 7. (a) Experimental (symbols) ⟨110⟩ hole inversion-layer mobility enhancement [4], [5] versus ⟨110⟩ uniaxial compressive stress on the (001) substrate. Calculation results in this paper (lines) are shown for comparison. The inset depicts the case of biaxial stress with the experimental data from [32] and [33]. (b) Corresponding calculated hole inversion-layer mobility enhancement values on the (110) substrate.

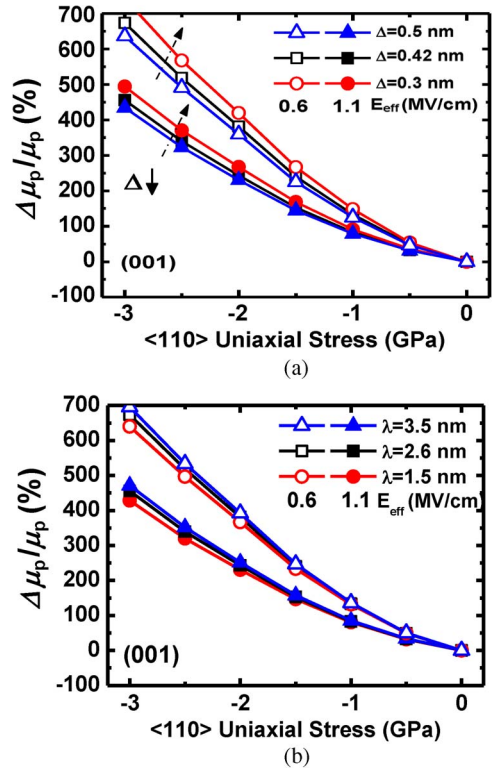

Fig. 8. Comparisons of the calculated hole inversion-layer mobility change versus ⟨110⟩ uniaxial compressive stress for varying (a) surface roughness RMS height and (b) surface roughness correlation length on the (001) substrate for two values of $E_{\rm eff}$.

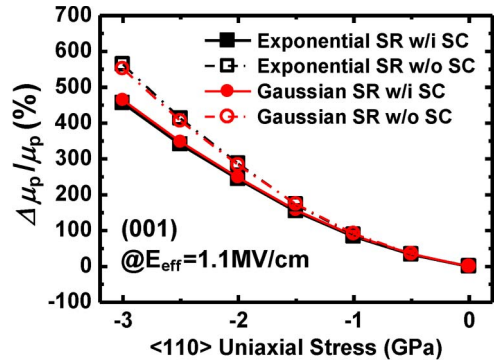

Fig. 9. Comparisons of the calculated hole inversion-layer mobility change between the exponential and Gaussian autocovariance functions with and without the screening effect on the (001) substrate under longitudinal compressive stress.

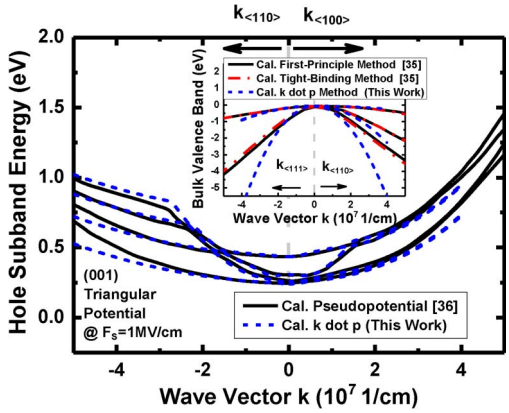

Fig. 10. Comparison of the calculated hole subband structure and bulk valence-band structure (in the inset) in this paper using the $k \cdot p$ method with those of the first-principles method [35], the tight-binding method [35], and the pseudopotential method [36].

Evidently, the calculated hole mobility change in Fig. 8(a) is almost the same as in Fig. 7. In other words, the uncertainty in Δ does not significantly affect the calculated hole mobility change. This also is the case for the surface roughness correlation length λ, as shown in Fig. 8(b), for Δ of 0.42 nm. Therefore, the extracted parameters, as listed in Table I, remain valid in the presence of uncertainty in the surface roughness parameters. Again, we add two interesting calculation results, as depicted in Fig. 9. First, the inclusion of the screening effect in surface roughness scattering will *reduce* the calculated hole inversion-layer mobility change, particularly in the high stress region. This means that the rate of increasing mobility due to stress is lowered if the screening effect is included. This may explain the observed deviation (see Fig. 1) from the calculated mobility enhancement of Wang *et al.* in the absence of the screened surface roughness scattering [8]. Second, a change in the surface roughness model from the exponential function to the Gaussian function does not influence the result.

Finally, we want to stress the validity of the strained $k \cdot p$ valence-band structure and the experimentally optimized deformation potentials aforementioned, particularly the primary factor d. First, the experimentally optimized d of -3.1 eV in this paper is exactly equal to that (-3.1 eV) [14] drawn from the cyclotron resonance measurements [34]. Second, in Fig. 10, we show a comparison of the valence-band structure and the hole subband structure obtained by performing the $k \cdot p$ calculation in this paper, the first-principles calculation [35], the tight-binding calculation [35], and the pseudopotential calculation [36]. Evidently, the $k \cdot p$ method can produce comparable band and subband structures of no more than 100 meV above the lowest one. The allowed window of 100 meV is much larger than the thermal energy of 26 meV times the degree of freedom of 2 in 2-D hole gas in near-equilibrium. Indeed, this window can be augmented if the population effect is taken into account. In a sense, the $k \cdot p$ method can reasonably work in the mobility calculation. As a consequence, the strained $k \cdot p$ valence-band structure with the optimized deformation potentials can ensure the accuracy of the calculated transport properties of 2-D hole gas under stress.

V. Conclusion

Sophisticated hole inversion-layer mobility calculations in the context of the strained $k \cdot p$ structure have been carried out. Calculated hole mobility change due to varying a_v, b, and d has been created and has accounted for 3-D uniaxial stress conditions. The primary factor d and the secondary factor b have been drawn. Guidelines have been established, followed by the experimental determination of a_v, b, and d. The literature errors of the Bir–Pikus deformation potentials have been improved, making possible the application of the strained $k \cdot p$ method in a real device by delivering the quantitatively correct transport properties of 2-D hole gas under stress.

References

[1] E. Bangert, K. von Klitzing, and G. Landwehr, "Self-consistent calculations of electric subbands in p-type silicon inversion layers," in *Proc. 12th Int. Conf. Phys. Semicond.*, M. H. Pilkuhn, Ed., Teubner, Stuttgart, 1974, pp. 714–718.

[2] F. J. Ohkawa and Y. Uemura, "Hartree approximation for the electronic structure of a p-channel inversion layer of silicon M.O.S.," *Prog. Theor. Phys. Supplement.*, no. 57, pp. 164–175, 1975. [Online]. Available: http://ptp.ipap.jp/journal/

[3] ITRS 2011. [Online]. Available: http://www.itrs.net

[4] L. Smith, V. Moroz, G. Eneman, P. Verheyen, F. Nouri, L. Washington, M. Jurczak, O. Penzin, D. Pramanik, and K. De Meyer, "Exploring the limits of stress-enhanced hole mobility," *IEEE Electron Device Lett.*, vol. 26, no. 9, pp. 652–654, Sep. 2005.

[5] L. Washington, F. Nouri, S. Thirupapuliyur, G. Eneman, P. Verheyen, V. Moroz, L. Smith, X. Xu, M. Kawaguchi, T. Huang, K. Ahmed, M. Balseanu, L. Q. Xia, M. Shen, Y. Kim, R. Rooyackers, K. De Meyer, and R. Schreutelkamp, "pMOSFET with 200% mobility enhancement induced by multiple stressors," *IEEE Electron Device Lett.*, vol. 27, no. 6, pp. 511–513, Jun. 2006.

[6] J. M. Luttinger and W. Kohn, "Motion of electrons and holes in perturbed periodic fields," *Phys. Rev.*, vol. 97, no. 4, pp. 869–883, Feb. 1955.

[7] G. L. Bir and G. E. Pikus, "Theory of the deformation potential for semiconductors with a complex band structure," *Sov. Phys. Solid State*, vol. 2, no. 9, pp. 2287–2300, Sep. 1960.

[8] E. X. Wang, P. Matagne, L. Shifren, B. Obradovic, R. Kotlyar, S. Cea, M. Stettler, and M. D. Giles, "Physics of hole transport in strained silicon MOSFET inversion layers," *IEEE Trans. Electron Devices*, vol. 53, no. 8, pp. 1840–1851, Aug. 2006.

[9] A. T. Pham, C. Jungemann, and B. Meinerzhagen, "Microscopic modeling of hole inversion layer mobility in unstrained and uniaxially stressed Si on arbitrarily oriented substrates," *Solid State Electron.*, vol. 52, no. 9, pp. 1437–1442, Sep. 2008.

[10] P. Packan, S. Cea, H. Deshpande, T. Ghani, M. Giles, O. Golonzka, M. Hattendorf, R. Kotlyar, K. Kuhn, A. Murthy, P. Ranade, L. Shifren, C. Weber, and K. Zawadzki, "High performance hi-$K+$ metal gate strain enhanced transistors on (110) silicon," in *IEDM Tech. Dig.*, 2008, pp. 63–66.

[11] F. M. Bufler, A. Erlebach, and M. Oulmane, "Hole mobility model with silicon inversion layer symmetry and stress-dependent piezoconductance coefficients," *IEEE Electron Device Lett.*, vol. 30, no. 9, pp. 996–998, Sep. 2009.
[12] Y. Sun, S. E. Thompson, and T. Nishida, "Physics of strain effects in semiconductors and metal–oxide–semiconductor field-effect transistors," *J. Appl. Phys.*, vol. 101, no. 10, pp. 104503-1–104503-22, May 2007.
[13] M. V. Fischetti and S. E. Laux, "Band structure, deformation potentials, and carrier mobility in strained Si, Ge, and SiGe alloys," *J. Appl. Phys.*, vol. 80, no. 4, pp. 2234–2252, Aug. 1996.
[14] R. Oberhuber, G. Zandler, and P. Vogl, "Subband structure and mobility of two-dimensional holes in strained Si/SiGe MOSFETs," *Phys. Rev. B, Condens. Matter*, vol. 58, no. 15, pp. 9941–9948, Oct. 1998.
[15] L. D. Laude, F. H. Pollak, and M. Cardona, "Effects of uniaxial stress on the indirect exciton spectrum of silicon," *Phys. Rev. B, Condens. Matter*, vol. 3, no. 8, pp. 2623–2636, Apr. 1971.
[16] M. Tiersten, "Acoustic-mode scattering mobility of holes in diamond type semiconductors," *J. Phys. Chem. Solids*, vol. 25, no. 11, pp. 1151–1168, Nov. 1964.
[17] P. Lawaetz, "Low-field mobility and galvanomagnetic properties of holes in germanium with phonon scattering," *Phys. Rev.*, vol. 174, no. 3, pp. 867–880, Oct. 1968.
[18] M. J. Chen, C. C. Lee, and K. H. Cheng, "Hole effective masses as a booster of self-consistent six-band $k \cdot p$ simulation in inversion layers of pMOSFETs," *IEEE Trans. Electron Devices*, vol. 58, no. 4, pp. 931–937, Apr. 2011.
[19] R. Kubo, "Statistical-mechanical theory of irreversible process. I," *J. Phys. Soc. Jpn.*, vol. 12, no. 6, pp. 570–586, Jun. 1957.
[20] D. A. Greenwood, "The Boltzmann equation in the theory of electrical conduction in metals," *Proc. Phys. Soc. Lond.*, vol. 71, no. 4, pp. 585–596, Apr. 1958.
[21] M. V. Fischetti, "Long-range Coulomb interactions in small Si devices. Part II. Effective electron mobility in thin-oxide structures," *J. Appl. Phys.*, vol. 89, no. 2, pp. 1232–1250, Jan. 2001.
[22] M. V. Fischetti, Z. Ren, P. M. Solomon, M. Yang, and K. Rim, "Six-band $k \cdot p$ calculation of the hole mobility in silicon inversion layers: Dependence on surface orientation, strain, and silicon thickness," *J. Appl. Phys.*, vol. 94, no. 2, pp. 1079–1095, Jul. 2003.
[23] J. D. Wiley, "Valence-band deformation potentials for the III–V compounds," *Solid State Commun.*, vol. 8, no. 22, pp. 1865–1868, Nov. 1970.
[24] M. Costato and L. Reggiani, "Scattering probabilities for holes I. Deformation potential and ionized impurity scattering mechanisms," *Phys. Stat. Sol. (B)*, vol. 58, no. 2, pp. 471–482, Aug. 1973.
[25] A. T. Pham, C. Jungemann, and B. Meinerzhagen, "Modeling of hole inversion layer mobility in unstrained and uniaxially strained Si on arbitrarily oriented substrates," in *Proc. ESSDERC*, 2007, pp. 390–393.
[26] M. De Michielis, D. Esseni, Y. L. Tsang, P. Palestri, L. Selmi, A. G. ONeill, and S. Chattopadhyay, "A semianalytical description of the hole band structure in inversion layers for the physically based modeling of pMOS transistors," *IEEE Trans. Electron Devices*, vol. 54, no. 9, pp. 2164–2173, Sep. 2007.
[27] S. Yamakawa, H. Ueno, K. Taniguchi, C. Hamaguchi, K. Miyatsuji, K. Masaki, and U. Ravaioli, "Study of interface roughness dependence of electron mobility in Si inversion layers using the Monte Carlo method," *J. Appl. Phys.*, vol. 79, no. 2, pp. 911–916, Jan. 1996.
[28] F. Gámiz, J. B. Roldán, J. A. López-Villanueva, P. Cartujo-Cassinello, and J. E. Carceller, "Surface roughness at the $Si-SiO_2$ interfaces in fully depleted silicon-on-insulator inversion layers," *J. Appl. Phys.*, vol. 86, no. 12, pp. 6854–6863, Dec. 1999.
[29] C. Jacoboni and L. Reggiani, "The Monte Carlo method for the solution of charge transport in semiconductors with applications to covalent materials," *Rev. Mod. Phys.*, vol. 55, no. 3, pp. 645–705, Jul.–Sep. 1983.
[30] C. J. Tang, S. H. Huang, T. Wang, and C. S. Chang, "Investigation of the strained PMOS on (110) substrate," in *International Symposium on VLSI Technology, Systems and Applications*, 2007, pp. 1–2.
[31] S. Takagi, A. Toriumi, M. Iwase, and H. Tango, "On the universality of inversion layer mobility in Si MOSFET's: Part I—Effects of substrate impurity concentration," *IEEE Trans. Electron Devices*, vol. 41, no. 12, pp. 2357–2362, Dec. 1994.
[32] K. Rim, K. Chan, L. Shi, D. Boyd, J. Ott, N. Klymko, F. Cardone, L. Tai, S. Koester, M. Cobb, D. Canaperi, B. To, E. Duch, I. Babich, R. Carruthers, P. Saunders, G. Walker, Y. Zhang, M. Steen, and M. Ieong, "Fabrication and mobility characteristics of ultrathin strained Si directly on insulator (SSDOI) MOSFETs," in *IEDM Tech. Dig.*, 2003, pp. 3.1.1–3.1.4.
[33] C. W. Leitz, M. T. Currie, M. L. Lee, Z.-Y. Cheng, D. A. Antoniadis, and E. A. Fitzgerald, "Hole mobility enhancements and alloy scattering-limited mobility in tensile strained Si/SiGe surface channel metal–oxide–semiconductor field-effect transistors," *J. Appl. Phys.*, vol. 92, no. 7, pp. 3745–3751, Oct. 2002.
[34] J. C. Hensel and G. Feher, "Cyclotron resonance experiments in uniaxially stressed silicon: Valence band inverse mass parameters and deformation potentials," *Phys. Rev.*, vol. 129, no. 3, pp. 1041–1062, Feb. 1963.
[35] Y. M. Niquet, D. Rideau, C. Tavernier, H. Jaouen, and X. Blasé, "Onsite matrix elements of the tight-binding Hamiltonian of a strained crystal: Application to silicon, germanium, and their alloys," *Phys. Rev. B, Condens. Matter*, vol. 79, no. 24, pp. 245201-1–245201-13, Jun. 2009.
[36] H. Nakatsuji, Y. Kamakura, and K. Taniguchi, "A study of subband structure and transport of two-dimensional hole in strained Si p-MOSFETs using full-band modeling," in *IEDM Tech. Dig.*, 2002, pp. 727–730.

Ming-Jer Chen (S'78–M'79–SM'98) received the Ph.D. degree from National Chiao Tung University (NCTU), Hsinchu, Taiwan, in 1985.

Since 1985, he has been a Professor with the Department of Electronics Engineering, NCTU.

Chien-Chih Lee received the Ph.D. degree in electronics engineering from National Chiao Tung University, Hsinchu, in 2012.

He is currently a principal R&D engineer in the Taiwan Semiconductor Manufacturing Company (TSMC), Hsinchu, Taiwan.

Wan-Li Chen received the M.S. degree in electronics engineering from National Chiao Tung University, Hsinchu, Taiwan, in 2012.

She is currently an R&D engineer in the Taiwan Semiconductor Manufacturing Company (TSMC), Hsinchu, Taiwan.